

Orthogonality sampling type methods for an inverse acoustic scattering problem

Dinh-Liem Nguyen*

Abstract

We consider the inverse acoustic scattering problem of determining the location and shape of penetrable scattering objects from multi-static Cauchy data of the scattered field. We propose two novel imaging functionals of orthogonality sampling type for solving the inverse problem. These imaging functionals, like the orthogonality sampling method, are fast, simple to implement, and robust with respect to noise in the data. A further advantage is that they are applicable to both near-field and far-field data. In particular, in the case of far-field data, the functionals can be easily modified such that only the scattered field data is needed. The theoretical analysis of the first imaging functional relies on the Factorization method along with the Funk-Hecke formula and a relation between the Cauchy data and the scattering amplitude of the scattered field. The second one is justified using the Helmholtz integral representation for the imaginary part of the Green's function of the direct scattering problem. Numerical examples are presented to illustrate the efficiency of the proposed imaging functionals.

Keywords. orthogonality sampling method, inverse scattering, near-field data, Cauchy data, Factorization method

AMS subject classification. 35R30, 35R09, 65R20

1 Introduction

We are concerned with the inverse medium scattering problem for the Helmholtz equation in \mathbb{R}^n ($n = 2$ or 3). This inverse problem can be considered as a model problem for the inverse scattering of time-harmonic acoustic waves or time-harmonic TE-polarized electromagnetic waves from bounded inhomogeneous media. It has been one of the central problems in inverse scattering theory and has a wide range of applications including nondestructive testing, radar imaging, medical imaging, and geophysical exploration [8]. Needless to say, there has been a large body of literature on both theoretical and numerical studies on this inverse problem, see [6, 8] and references therein.

In the present paper, we are interested in determining the location and shape of scattering objects from (near-field or far-field) multi-static data of the scattered field. Since we study sampling methods to numerically solve this inverse problem, we will mainly discuss related results in this direction. The Linear Sampling Method (LSM) can be considered as the first sampling method

*Department of Mathematics, Kansas State University, Manhattan, KS 66506, USA; (dlnghuyen@ksu.edu).

developed to solve the inverse problem under consideration [7]. The LSM aims to construct an indicator function for unknown scattering objects. This indicator function is evaluated on sampling points obtained by discretizing some domain in which the unknown target is searched for. The evaluation of this indicator function is typically fast, non-iterative and its construction does not require advanced a priori information about the unknown target. These are also the main advantages of the LSM over nonlinear optimization-based methods in solving inverse scattering problems. Shortly after the finding of the LSM, other sampling type methods for inverse problems including the point source method [24], the Factorization method (FM) [18], the probe method [13] were also developed. We refer to [25] for a discussion on sampling and probe methods studied until 2006. These methods have been later extended to solve various inverse problems, see [4, 19, 25] and references therein.

Our work in this paper is inspired by a class of sampling methods that have been studied more recently. We are particularly interested in the orthogonality sampling method (OSM) proposed in [26]. While inheriting the advantages of the classical sampling methods mentioned above, the OSM is particularly attractive thanks to its simplicity and efficiency. For instance, the implementation of the OSM only involves an evaluation of an inner product or some double integral (no regularization is needed). The method is extremely robust with respect to noise in the data and its stability can be easily justified. However, the theoretical analysis of the OSM is far less developed compared with that of the classical sampling methods, especially the FM and LSM. The original paper [26] justifies the OSM for small scattering objects using one-wave data. Its multi-frequency version has been theoretically investigated in [10]. The theoretical analysis of the OSM for extended scatterers using multi-static data has been studied in [21] via an equivalent relation between the OSM and a direct sampling method. The OSM has been recently extended to Maxwell's equations for one-wave data and multi-static data in [12, 22]. We also refer to [11, 14–17, 21, 23] for studies on direct sampling methods (DSM) which are closely related to the OSM. We note that the DSM studied in [14, 15, 17, 23] and related works aims to reconstruct only thin and small scattering objects. And to our knowledge, most of the works for the OSM and DSM have been studied for inverse scattering problems with far-field data. The data is either the scattering amplitude of the scattered field or the scattered field measured on some boundary that is far away from unknown targets. The latter is typically the case when the well known Helmholtz-Kirchhoff identity is used to justify the sampling method, see for instance [14, 15, 17].

We propose in this paper two novel imaging functionals for solving the inverse problem of interest. These imaging functionals are inspired by the OSM. While having all the advantages of the OSM originally studied in [26], these imaging functionals can image extended scattering objects, and are applicable to both near-field and far-field data. More precisely, our imaging functionals use (near-field or far-field) boundary Cauchy data. Moreover, they can also be easily modified to use only the scattered field data in the case of far-field measurements. We study the theoretical analysis of the first imaging functional using the analysis of Factorization method and the Funk-Hecke formula. The idea is to use a relation between the Cauchy data and the scattering amplitude of the scattered field. This relation allows us to rewrite our imaging functional as $\|F\varphi_z\|^2$ where F is the far-field operator and φ_z is some special test function. Then using a factorization of F , analytical properties of the operators in the factorization and the Funk-Hecke formula it can be justified that the imaging functional can work as an approximate indicator function for the

unknown scattering object. We also refer to [21] for using the Factorization method to justify a direct sampling method.

The theoretical analysis of the second imaging functional relies on the Helmholtz integral representation of the imaginary part of the Green's function of the direct scattering problem. The representation allows us to show that the second imaging functional is equal to a functional that involves $\text{sinc}(|y - z|)$ where $z \in \mathbb{R}^n$ is a sampling point and the point y is inside the unknown scatterer. This sinc function is the main ingredient for justifying the behavior of the imaging functional. Transforming an imaging functional into some functional involving the sinc function using the Helmholtz-Kirchhoff identity has been done for the justification of the direct sampling method, see, e.g. [14, 15, 17], and also the time reverse migration technique [5, 9]. However, our approach in this paper for the second imaging functional does not rely on the Helmholtz-Kirchhoff identity and therefore avoids the assumption that the measurement has to be taken far away from the unknown scattering object. Another way to avoid using the Helmholtz-Kirchhoff identity for the OSM can be found in [1] for a 2D inverse scattering problem.

It can be seen from our numerical study that the new imaging functionals work very efficiently for both near field and far field data, and are extremely robust with respect to noise in the data. Also, although the formulae of the imaging functionals are not similar and their justifications are completely different, the reconstruction results obtained from the two imaging functionals are quite similar. However, it is still an open question whether there is an equivalent relation between these two functionals. Using the analysis of the Factorization method, the justification of the first imaging functional is more satisfactory compared with that of the second one since the effect of using multiple incident waves is not really reflected in the justification of the second imaging functional. However, we have to assume that the wave number is not an interior transmission eigenvalue in order to apply the analysis of the Factorization method (see in addition Assumption 1).

The paper is organized as follows. We will formulate the inverse scattering problem of interest and an analysis of the Factorization method in Section 2. The formulae, theoretical analysis and stability estimates of the first and second imaging functionals are respectively presented in Sections 3 and 4. Section 5 is dedicated to a numerical study of the imaging functionals.

2 The inverse scattering problem and Factorization method

In this section we formulate the inverse problem we want to solve and recall some necessary ingredients of the Factorization method for the theoretical analysis of our imaging functionals. Consider a penetrable inhomogeneous medium that occupies a bounded Lipschitz domain $D \subset \mathbb{R}^n$ ($n = 2$ or 3). Assume that this medium is characterized by the bounded function $\eta(y)$ and that $\eta = 0$ in $\mathbb{R}^n \setminus \overline{D}$. Consider the incident plane wave

$$u_{\text{in}}(x, d) = e^{ikx \cdot d}, \quad x \in \mathbb{R}^n, \quad d \in \mathbb{S}^{n-1} := \{x \in \mathbb{R}^n : |x| = 1\},$$

where $k > 0$ is the wave number and d is the direction vector of propagation. We consider the following model problem for the scattering of $u_{\text{in}}(x, d)$ by the inhomogeneous medium

$$\Delta u + k^2(1 + \eta(x))u = 0, \quad x \in \mathbb{R}^n, \quad (1)$$

$$u = u_{\text{sc}} + u_{\text{in}}, \quad (2)$$

$$\lim_{r \rightarrow \infty} r^{\frac{n-1}{2}} \left(\frac{\partial u_{\text{sc}}}{\partial r} - ik u_{\text{sc}} \right) = 0, \quad r = |x|, \quad (3)$$

where $u(x, d)$ is the total field, $u_{\text{sc}}(x, d)$ is the scattered field, and the Sommerfeld radiation condition (3) holds uniformly for all directions $x/|x| \in \mathbb{S}^{n-1}$. If $\mathbb{R}^n \setminus \overline{D}$ is connected and $\text{Im}(\eta) \geq 0$, this scattering problem is known to have a unique weak solution $u_{\text{sc}} \in H_{\text{loc}}^1(\mathbb{R}^n)$, see [8].

Inverse problem. Consider a domain $\Omega \subset \mathbb{R}^n$ such that $D \subset \Omega$ and denote by $\nu(x)$ the outward normal unit vector to $\partial\Omega$ at x . We aim to determine D from $u_{\text{sc}}(x, d)$ and $\partial u_{\text{sc}}(x, d)/\nu(x)$ for all $(x, d) \in \partial\Omega \times \mathbb{S}^{n-1}$.

We denote by $\Phi(x, y)$ the free-space Green's function of the scattering problem (1)–(3). It is well known that

$$\Phi(x, y) = \begin{cases} \frac{i}{4} H_0^{(1)}(k|x-y|), & \text{in } \mathbb{R}^2, \\ \frac{e^{ik|x-y|}}{4\pi|x-y|}, & \text{in } \mathbb{R}^3. \end{cases} \quad (4)$$

It is also well known that problem (1)–(3) is equivalent to the Lippmann-Schwinger equation

$$u_{\text{sc}}(x) = \int_D \Phi(x, y) \eta(y) u(y) dy, \quad (5)$$

and that the scattered field has the asymptotic behavior

$$u_{\text{sc}}(x, d) = \frac{e^{ik|x|}}{|x|^{(n-1)/2}} (u^\infty(\hat{x}, d) + O(1/|x|)), \quad |x| \rightarrow \infty,$$

for all $(\hat{x}, d) \in \mathbb{S}^{n-1} \times \mathbb{S}^{n-1}$. The function $u^\infty(\hat{x}, d)$ is called the scattering amplitude or the far-field pattern of the scattered field u_{sc} . Let $F : L^2(\mathbb{S}^{n-1}) \rightarrow L^2(\mathbb{S}^{n-1})$ be the far-field operator defined by

$$Fg(\hat{x}) = \int_{\mathbb{S}^{n-1}} u^\infty(\hat{x}, d) g(d) ds(d).$$

Thanks to the well-posedness of the scattering problem (1)–(3) we can define the solution operator $G : L^2(D) \rightarrow L^2(\mathbb{S}^{n-1})$ as

$$Gf = w^\infty,$$

where w^∞ is the scattering amplitude of the unique solution w to

$$\Delta w + k^2(1 + \eta)w = -k^2 \eta f, \quad \text{in } \mathbb{R}^n, \quad (6)$$

$$\lim_{r \rightarrow \infty} r^{\frac{n-1}{2}} \left(\frac{\partial w}{\partial r} - ikw \right) = 0, \quad r = |x|. \quad (7)$$

Note that this problem is just problem (1)–(3) rewritten for the scattered field with incident field u_{in} replaced by f . By linearity of problem (1)–(3), Fg is just the scattering amplitude of solution w to problem (6)–(7) with $f = v_g$, defined by

$$v_g(x) = \int_{\mathbb{S}^{n-1}} e^{ikx \cdot d} g(d) ds(d), \quad g \in L^2(\mathbb{S}^{n-1}), \quad x \in \mathbb{R}^n.$$

Now we define the compact operator $H : L^2(\mathbb{S}^{n-1}) \rightarrow L^2(D)$ as $Hg = v_g|_D$. Then obviously the far-field operator can be factorized as

$$F = GH.$$

Let $H^* : L^2(D) \rightarrow L^2(\mathbb{S}^{n-1})$ be the adjoint of H given by

$$H^*g(\hat{x}) = \int_{\mathbb{S}^{n-1}} e^{-ik\hat{x} \cdot y} g(y) ds(y),$$

and we define $T : L^2(D) \rightarrow L^2(D)$ as

$$Tf = k^2 \eta(f + w), \tag{8}$$

where w solves problem (6)–(7). Since w solves the Lippmann-Schwinger equation, we have

$$w^\infty(\hat{x}) = k^2 \int_D e^{-ik\hat{x} \cdot y} \eta(y)(w(y) + f(y)) dy,$$

which leads to the factorizations

$$G = H^*T, \quad F = H^*TH.$$

To proceed further with the analysis of the Factorization method we need to briefly discuss the interior transmission eigenvalues. We call $k > 0$ an interior transmission eigenvalue if the problem

$$\begin{aligned} \Delta u + k^2(1 + \eta)u &= 0, \quad \text{in } D \\ \Delta v + k^2v &= 0, \quad \text{in } D \\ u &= v, \quad \frac{\partial u}{\partial \nu} = \frac{\partial v}{\partial \nu}, \quad \text{on } \partial D \end{aligned}$$

has a nontrivial solution $(u, v) \in L^2(D) \times L^2(D)$ such that $u - v \in H^2(D)$.

It is known that the set of real transmission eigenvalues is at most discrete. See [3] and the references therein for the analysis of transmission eigenvalue problems. For the next results, we assume that k is not an interior transmission eigenvalue. The following assumption is also important for the Factorization method analysis.

Assumption 1. *We assume that $\eta \in L^\infty(\mathbb{R}^n)$, $\text{Im}(\eta) \geq 0$ and that there exists a constant $c > 0$ such that $\text{Re}(\eta(x)) + \text{Im}(\eta(x)) \geq c$ for almost all $x \in D$.*

The following theorem of the Factorization method is important to the theoretical analysis of the imaging functional studied in this section, see [2] for a proof of the theorem.

Theorem 2. a) Let

$$\varphi_z(d) = e^{-ikz \cdot d}, \quad z \in \mathbb{R}^n, \quad d \in \mathbb{S}^{n-1}. \quad (9)$$

Then $\varphi_z \in \text{Range}(H^*)$ if and only if $z \in D$.

b) If Assumption 1 holds true, then operator T defined in (8) satisfies the coercivity property. That means there exists a constant $c > 0$ such that

$$|\langle Tf, f \rangle| \geq c \|f\|^2, \quad \text{for all } f \in \text{Range}(H).$$

3 The imaging functional $I(z)$

We define the imaging functional $I(z)$ as

$$I(z) := \int_{\mathbb{S}^{n-1}} \left| \int_{\mathbb{S}^{n-1}} \int_{\partial\Omega} u_{\text{sc}}(y, d) \frac{\partial \Phi^\infty(\hat{x}, y)}{\partial \nu(y)} - \frac{\partial u_{\text{sc}}(y, d)}{\partial \nu(y)} \Phi^\infty(\hat{x}, y) ds(y) \varphi_z(d) ds(d) \right|^2 ds(\hat{x}) \quad (10)$$

where φ_z is given in (9) and $\Phi^\infty(\hat{x}, y)$ is the scattering amplitude of the Green's function $\Phi(x, y)$, given by

$$\Phi^\infty(\hat{x}, y) = \begin{cases} \frac{e^{i\pi/4}}{\sqrt{8\pi k}} e^{-ik\hat{x} \cdot y}, & \text{in } \mathbb{R}^2, \\ \frac{1}{4\pi} e^{-ik\hat{x} \cdot y}, & \text{in } \mathbb{R}^3. \end{cases}$$

The next theorem justifies the behavior of the imaging functional $I(z)$.

Theorem 3. Assume that k is not an interior transmission eigenvalue and that Assumption 1 holds true. Then the imaging functional $I(z)$ satisfies

$$\begin{aligned} I(z) &\geq \gamma_z > 0, \quad \text{for } z \in D, \quad \text{and} \\ I(z) &= O\left(\frac{1}{\text{dist}(z, D)^{n-1}}\right) \quad \text{as } \text{dist}(z, D) \rightarrow \infty, \quad \text{for } z \notin D, \end{aligned}$$

where $\text{dist}(z, D)$ is the distance from z to D .

Proof. From the Helmholtz integral representation for u_{sc} we have

$$u_{\text{sc}}(x, d) = \int_{\partial\Omega} u_{\text{sc}}(y, d) \frac{\partial \Phi(x, y)}{\partial \nu(y)} - \frac{\partial u_{\text{sc}}(y, d)}{\partial \nu(y)} \Phi(x, y) ds(y),$$

which implies that

$$u^\infty(\hat{x}, d) = \int_{\partial\Omega} u_{\text{sc}}(y, d) \frac{\partial \Phi^\infty(\hat{x}, y)}{\partial \nu(y)} - \frac{\partial u_{\text{sc}}(y, d)}{\partial \nu(y)} \Phi^\infty(\hat{x}, y) ds(y).$$

Then substituting this formula of u^∞ in the far-field operator F implies that

$$F\varphi_z(\hat{x}) = \int_{\mathbb{S}^{n-1}} \int_{\partial\Omega} u_{\text{sc}}(y, d) \frac{\partial \Phi^\infty(\hat{x}, y)}{\partial \nu(y)} - \frac{\partial u_{\text{sc}}(y, d)}{\partial \nu(y)} \Phi^\infty(\hat{x}, y) ds(y) \varphi_z(d) ds(d).$$

Therefore

$$I(z) = \int_{\mathbb{S}^{n-1}} |F\varphi_z(\hat{x})|^2 ds(\hat{x}) = \|F\varphi_z\|^2.$$

Since $\|\varphi_z\|^2 = \int_{\mathbb{S}^{n-1}} |e^{-ikz \cdot d}|^2 ds(d) = |\mathbb{S}^{n-1}|$ (the surface area of \mathbb{S}^{n-1}), we have

$$\sqrt{|\mathbb{S}^{n-1}|} \|F\varphi_z\| \geq \langle F\varphi_z, \varphi_z \rangle = \langle H^*TH\varphi_z, \varphi_z \rangle = \langle TH\varphi_z, H\varphi_z \rangle$$

Using the coercivity of T in Theorem 2 and $\|F\varphi_z\| \leq \|G\| \|H\varphi_z\|$ we obtain

$$\frac{c^2}{|\mathbb{S}^{n-1}|} \|H\varphi_z\|^4 \leq I(z) \leq \|G\|^2 \|H\varphi_z\|^2,$$

where c is the constant from the coercivity of T in Theorem 2. Now let $z \in \Omega$. Then by Theorem 2 again we have $\varphi_z \in \text{Range}(H^*)$ which implies that $\varphi_z = H^*h_z$ for some $h_z \neq 0$. We estimate

$$\|H\varphi_z\| \geq \frac{\langle H\varphi_z, h_z \rangle}{\|h_z\|} = \frac{\langle \varphi_z, H^*h_z \rangle}{\|h_z\|} = \frac{|\mathbb{S}^{n-1}|}{\|h_z\|} > 0.$$

This deduces that $I(z) > \gamma_z$ for $z \in D$ with $\gamma_z = c^2 |\mathbb{S}^{n-1}|^3 / \|h_z\|^4$.

Now for $z \notin D$, using the Funk-Hecke formula (see [8]) we obtain

$$H\varphi_z(x) = \int_{\mathbb{S}^{n-1}} e^{-ik(z-x) \cdot d} ds(d) = \begin{cases} 2\pi J_0(k|z-x|), & \text{in } \mathbb{R}^2, \\ 4\pi j_0(k|z-x|), & \text{in } \mathbb{R}^3. \end{cases} \quad (11)$$

Therefore, using the asymptotic behavior of $J_0(r) = O(1/\sqrt{r})$ and $j_0(r) = O(1/r)$ as $r \rightarrow \infty$ we obtain that

$$\|H\varphi_z\|^2 = O\left(\frac{1}{\text{dist}(z, D)^{n-1}}\right), \quad \text{as } \text{dist}(z, D) \rightarrow \infty.$$

This completes the proof. \square

In practice the data are always perturbed with some noise. We assume the noisy data u_{sc}^δ and $\partial u_{\text{sc}}^\delta / \partial \nu$ satisfy

$$\|u_{\text{sc}} - u_{\text{sc}}^\delta\|_{L^2(\partial\Omega \times \mathbb{S}^{n-1})} \leq \delta_1 \|u_{\text{sc}}\|_{L^2(\partial\Omega \times \mathbb{S}^{n-1})}, \quad (12)$$

$$\left\| \frac{\partial u_{\text{sc}}}{\partial \nu} - \frac{\partial u_{\text{sc}}^\delta}{\partial \nu} \right\|_{L^2(\partial\Omega \times \mathbb{S}^{n-1})} \leq \delta_2 \left\| \frac{\partial u_{\text{sc}}}{\partial \nu} \right\|_{L^2(\partial\Omega \times \mathbb{S}^{n-1})}, \quad (13)$$

for some positive constants δ_1, δ_2 . We now give a stability estimate for the imaging functional $I(z)$.

Theorem 4 (stability estimate). *Denote by $I^\delta(z)$ the imaging functional corresponding to noisy data u_{sc}^δ and $\partial u_{\text{sc}}^\delta / \partial \nu$. Then*

$$I(z) - I^\delta(z) \leq \mathcal{C} (2 \max(\delta_1, \delta_2) + \max(\delta_1^2, \delta_2^2)), \quad \text{for all } z \in \mathbb{R}^3,$$

where

$$\mathcal{C} = |\mathbb{S}^{n-1}|^2 \left(\|\Phi^\infty\|_{L^2(\partial\Omega \times \mathbb{S}^{n-1})}^2 + \left\| \frac{\partial \Phi^\infty}{\partial \nu} \right\|_{L^2(\partial\Omega \times \mathbb{S}^{n-1})}^2 \right) \left(\|u_{\text{sc}}\|_{L^2(\partial\Omega \times \mathbb{S}^{n-1})}^2 + \left\| \frac{\partial u_{\text{sc}}}{\partial \nu} \right\|_{L^2(\partial\Omega \times \mathbb{S}^{n-1})}^2 \right).$$

Proof. Let $u^{\infty,\delta}(\hat{x}, d)$ and F^δ be the scattering amplitude and the far-field operator for noisy Cauchy data. That means

$$u^{\infty,\delta}(\hat{x}, d) = \int_{\partial\Omega} u_{\text{sc}}^\delta(y, d) \frac{\partial \Phi^\infty(\hat{x}, y)}{\partial \nu(y)} - \frac{\partial u_{\text{sc}}^\delta(y, d)}{\partial \nu(y)} \Phi^\infty(\hat{x}, y) ds(y) \quad (14)$$

$$F^\delta \varphi_z(\hat{x}) = \int_{\mathbb{S}^{n-1}} u^{\infty,\delta}(\hat{x}, d) \varphi_z(d) ds(d). \quad (15)$$

Using the Cauchy-Schwarz inequality we have

$$|u^\infty(\hat{x}, d) - u^{\infty,\delta}(\hat{x}, d)| \leq \|(u_{\text{sc}} - u_{\text{sc}}^\delta)(\cdot, d)\| \left\| \frac{\partial \Phi^\infty(\hat{x}, \cdot)}{\partial \nu(y)} \right\| + \left\| \frac{\partial(u_{\text{sc}} - u_{\text{sc}}^\delta)(\cdot, d)}{\partial \nu(y)} \right\| \|\Phi^\infty(\hat{x}, \cdot)\|,$$

and hence

$$\begin{aligned} & |u^\infty(\hat{x}, d) - u^{\infty,\delta}(\hat{x}, d)|^2 \\ & \leq \left(\|(u_{\text{sc}} - u_{\text{sc}}^\delta)(\cdot, d)\|^2 + \left\| \frac{\partial(u_{\text{sc}} - u_{\text{sc}}^\delta)(\cdot, d)}{\partial \nu(y)} \right\|^2 \right) \left(\|\Phi^\infty(\hat{x}, \cdot)\|^2 + \left\| \frac{\partial \Phi^\infty(\hat{x}, \cdot)}{\partial \nu(y)} \right\|^2 \right). \end{aligned}$$

Let $C = \|\Phi^\infty\|_{L^2(\partial\Omega \times \mathbb{S}^{n-1})}^2 + \|\partial \Phi^\infty / \partial \nu\|_{L^2(\partial\Omega \times \mathbb{S}^{n-1})}^2$. This leads to

$$\begin{aligned} \|u^\infty - u^{\infty,\delta}\|_{L^2(\mathbb{S}^{n-1} \times \mathbb{S}^{n-1})}^2 & \leq C \left(\|u_{\text{sc}} - u_{\text{sc}}^\delta\|_{L^2(\partial\Omega \times \mathbb{S}^{n-1})}^2 + \left\| \frac{\partial(u_{\text{sc}} - u_{\text{sc}}^\delta)}{\partial \nu(y)} \right\|_{L^2(\partial\Omega \times \mathbb{S}^{n-1})}^2 \right) \\ & \leq C \left(\delta_1^2 \|u_{\text{sc}}\|_{L^2(\partial\Omega \times \mathbb{S}^{n-1})}^2 + \delta_2^2 \left\| \frac{\partial u_{\text{sc}}}{\partial \nu} \right\|_{L^2(\partial\Omega \times \mathbb{S}^{n-1})}^2 \right), \end{aligned}$$

which implies that

$$\|F\varphi_z - F^\delta \varphi_z\|^2 \leq C |\mathbb{S}^{n-1}|^2 \max(\delta_1^2, \delta_2^2) \left(\|u_{\text{sc}}\|_{L^2(\partial\Omega \times \mathbb{S}^{n-1})}^2 + \left\| \frac{\partial u_{\text{sc}}}{\partial \nu} \right\|_{L^2(\partial\Omega \times \mathbb{S}^{n-1})}^2 \right).$$

Similarly we also have

$$\|F\varphi_z\|^2 \leq C |\mathbb{S}^{n-1}|^2 \left(\|u_{\text{sc}}\|_{L^2(\partial\Omega \times \mathbb{S}^{n-1})}^2 + \left\| \frac{\partial u_{\text{sc}}}{\partial \nu} \right\|_{L^2(\partial\Omega \times \mathbb{S}^{n-1})}^2 \right).$$

Using $I(z) = \|F\varphi_z\|^2$ and the triangle inequality we have

$$\begin{aligned} I(z) - I^\delta(z) & = \|F\varphi_z\|^2 - \|F^\delta \varphi_z\|^2 \leq \|F\varphi_z - F^\delta \varphi_z\| \left(\|F\varphi_z\| + \|F^\delta \varphi_z\| \right) \\ & \leq 2 \|F\varphi_z\| \|F\varphi_z - F^\delta \varphi_z\| + \|F\varphi_z - F^\delta \varphi_z\|^2 \\ & \leq C |\mathbb{S}^{n-1}|^2 \left(\|u_{\text{sc}}\|_{L^2(\partial\Omega \times \mathbb{S}^{n-1})}^2 + \left\| \frac{\partial u_{\text{sc}}}{\partial \nu} \right\|_{L^2(\partial\Omega \times \mathbb{S}^{n-1})}^2 \right) \left(2\sqrt{\max(\delta_1^2, \delta_2^2)} + \max(\delta_1^2, \delta_2^2) \right). \end{aligned}$$

proving the theorem. \square

Remark 5. We note that if the measurements are taken far away from the scattering medium, by the radiation condition we can replace $\partial u_{\text{sc}}/\partial \nu$ by iku_{sc} in the imaging functional $I(z)$. Then the modified imaging functional

$$I_{\text{far}}(z) := \int_{\mathbb{S}^{n-1}} \left| \int_{\mathbb{S}^{n-1}} \int_{\partial\Omega} u_{\text{sc}}(y, d) \frac{\partial \Phi^\infty(\hat{x}, y)}{\partial \nu(y)} - iku_{\text{sc}}(y, d) \Phi^\infty(\hat{x}, y) \text{d}s(y) \varphi_z(d) \text{d}s(d) \right|^2 \text{d}s(\hat{x}) \quad (16)$$

only needs the scattered field data $u_{\text{sc}}(x, d)$ and approximates the imaging functional $I(z)$.

4 The imaging functional $I_2(z)$

We define our second imaging functional as

$$I_2(z) := \int_{\mathbb{S}^{n-1}} \left| \int_{\partial\Omega} \left(\frac{\partial \text{Im} \Phi(x, z)}{\partial \nu(x)} u_{\text{sc}}(x, d) - \text{Im} \Phi(x, z) \frac{\partial u_{\text{sc}}(x, d)}{\partial \nu(x)} \right) \text{d}s(x) \right|^2 \text{d}s(d), \quad (17)$$

where $\Phi(x, z)$ is the Green's function given in (4).

Theorem 6. The imaging functional I_2 satisfies

$$I_2(z) = \int_{\mathbb{S}^{n-1}} \left| k^2 \int_D \text{Im} \Phi(y, z) \eta(y) u(y, d) \text{d}y \right|^2 \text{d}s(d).$$

where

$$\text{Im} \Phi(y, z) = \begin{cases} J_0(k|z - y|), & \text{in } \mathbb{R}^2, \\ \frac{k}{4\pi} j_0(k|z - y|), & \text{in } \mathbb{R}^3. \end{cases} \quad (18)$$

Proof. We have from the Lippmann-Schwinger equation that

$$u_{\text{sc}}(x, d) = k^2 \int_D \Phi(x, y) \eta(y) u(y, d) \text{d}y, \quad \frac{\partial u_{\text{sc}}(x, d)}{\partial \nu(x)} = k^2 \int_D \frac{\partial \Phi(x, y)}{\partial \nu(x)} \eta(y) u(y, d) \text{d}y.$$

Therefore, we have that

$$\begin{aligned} & \int_{\partial\Omega} \left(\frac{\partial \text{Im} \Phi(x, z)}{\partial \nu(x)} u_{\text{sc}}(x, d) - \text{Im} \Phi(x, z) \frac{\partial u_{\text{sc}}(x, d)}{\partial \nu(x)} \right) \text{d}s(x) \\ &= \int_{\partial\Omega} \left(\frac{\partial \text{Im} \Phi(x, z)}{\partial \nu(x)} k^2 \int_D \Phi(x, y) \eta(y) u(y, d) \text{d}y - \text{Im} \Phi(x, z) k^2 \int_D \frac{\partial \Phi(x, y)}{\partial \nu(x)} \eta(y) u(y, d) \text{d}y \right) \text{d}s(x) \\ &= k^2 \int_{\partial\Omega} \int_D \left(\frac{\partial \text{Im} \Phi(x, z)}{\partial \nu(x)} \Phi(x, y) - \text{Im} \Phi(x, z) \frac{\partial \Phi(x, y)}{\partial \nu(x)} \right) \eta(y) u(y, d) \text{d}y \text{d}s(x) \\ &= k^2 \int_D \int_{\partial\Omega} \left(\frac{\partial \text{Im} \Phi(x, z)}{\partial \nu(x)} \Phi(y, x) - \text{Im} \Phi(x, z) \frac{\partial \Phi(y, x)}{\partial \nu(x)} \right) \text{d}s(x) \eta(y) u(y, d) \text{d}y. \end{aligned} \quad (19)$$

Since $\Delta \text{Im} \Phi(z, y) + k^2 \text{Im} \Phi(z, y) = 0$ for all $z, y \in \mathbb{R}^n$, we have from the Helmholtz integral representation that

$$\int_{\partial\Omega} \left(\frac{\partial \text{Im} \Phi(x, z)}{\partial \nu(x)} \Phi(y, x) - \text{Im} \Phi(x, z) \frac{\partial \Phi(y, x)}{\partial \nu(x)} \right) \text{d}s(x) = \text{Im} \Phi(y, z).$$

Therefore, substituting this identity in (19) implies

$$\int_{\partial\Omega} \left(\frac{\partial \operatorname{Im} \Phi(x, z)}{\partial \nu(x)} u_{\text{sc}}(x, d) - \operatorname{Im} \Phi(x, z) \frac{\partial u_{\text{sc}}(x, d)}{\partial \nu(x)} \right) ds(x) = k^2 \int_D \operatorname{Im} \Phi(y, z) \eta(y) u(y, d) dy.$$

Now the proof can be completed by substituting this equation in (17). \square

Using the asymptotic behavior of $J_0(k|y - z|)$ and $j_0(k|y - z|)$ as $|y - z| \rightarrow \infty$ we can easily estimate, for $z \notin D$, that

$$I_2(z) = O\left(\frac{1}{\operatorname{dist}(z, D)^{n-1}}\right) \text{ as } \operatorname{dist}(z, D) \rightarrow \infty.$$

For $z \in D$, $I_2(z)$ is supposed to have finite positive values because $J_0(k|y - z|)$ and $j_0(k|y - z|)$ peak when $k|y - z| \approx 0$.

Like in the stability study of the first imaging functional we can estimate

$$I_2(z) - I_2^\delta(z) \leq C \max(\delta_1^2, \delta_2^2), \quad \text{for all } z \in \mathbb{R}^n,$$

where δ_1 and δ_2 are the noise levels in the Cauchy data given in (12)–(13) and

$$C = \left(\|\operatorname{Im} \Phi\|_{L^2(\partial\Omega \times \mathbb{S}^{n-1})}^2 + \left\| \frac{\partial \operatorname{Im} \Phi}{\partial \nu} \right\|_{L^2(\partial\Omega \times \mathbb{S}^{n-1})}^2 \right) \left(\|u_{\text{sc}}\|_{L^2(\partial\Omega \times \mathbb{S}^{n-1})}^2 + \left\| \frac{\partial u_{\text{sc}}}{\partial \nu} \right\|_{L^2(\partial\Omega \times \mathbb{S}^{n-1})}^2 \right).$$

This estimate implies the stability of the imaging functional I_2 with respect to noise in the data.

Remark 7. *As in the case of imaging functional $I(z)$, we can also modify $I_2(z)$ to handle only the scattered field data $u_{\text{sc}}(x, d)$ that is measured far away from the scattering medium as follows*

$$I_{2,\text{far}}(z) := \int_{\mathbb{S}^{n-1}} \left| \int_{\partial\Omega} \left(\frac{\partial \operatorname{Im} \Phi(x, z)}{\partial \nu(x)} u_{\text{sc}}(x, d) - ik \operatorname{Im} \Phi(x, z) u_{\text{sc}}(x, d) \right) ds(x) \right|^2 ds(d). \quad (20)$$

Furthermore, to use point sources instead of incident plane waves we can just replace \mathbb{S}^{n-1} in the first integral of I_2 or $I_{2,\text{far}}$ by some boundary or surface where the sources are located.

5 Numerical examples

We present in this section several numerical examples in 2D to illustrate the performance of the proposed imaging functionals $I(z)$ and $I_2(z)$. More precisely, we will examine the performance of these functionals for data with different wave numbers (Figure 1), highly noisy data (Figure 2), far-field data (Figure 3), and partial data (Figure 4). Reconstruction results using the imaging functionals $I_{\text{far}}(z)$ and $I_{2,\text{far}}(z)$ are also presented in the case of far-field data. As we can see in the pictures below, the reconstruction results obtained from $I(z)$ and $I_2(z)$ are very similar. Therefore, we will present more results of $I(z)$ and skip some of the results of $I_2(z)$ to avoid repetition of similar pictures. For the pictures in this section, the imaging functionals are scaled by dividing by their maximal values.

The following common parameters and notations are used in the numerical examples

$$\begin{aligned}
&\text{Sampling domain} = (-2, 2) \times (-2, 2), \\
&\text{Number of sampling points} = 96^2, \\
&\partial\Omega = \{(x_1, x_2)^\top \in \mathbb{R}^2 : x_1^2 + x_2^2 = R^2\}, \\
&\text{Near-field data: } R = 3, \\
&\text{Far-field data: } R = 100, \\
&\text{Number of data points on } \partial\Omega: N_x, \\
&\text{Number of incident plane waves: } N_d.
\end{aligned}$$

The following scattering objects are considered in the numerical examples.

a) Kite-shaped object

$$\begin{aligned}
\partial D &= \{x \in \mathbb{R}^2 : x = ((\cos(t) + 0.65 \cos(2t) - 0.65)/2, 1.5 \sin(t)/2.5)^\top, 0 \leq t \leq 2\pi\}, \\
\eta(x) &= 0.5 + 0.1i \quad \text{in } D.
\end{aligned}$$

b) Disk-and-rectangle object

$$\begin{aligned}
\text{disk} &= \{(x_1, x_2)^\top \in \mathbb{R}^2 : (x_1 + 0.6)^2 + (x_2 - 0.6)^2 < 0.4^2\}, \\
\text{rectangle} &= \{(x_1, x_2)^\top \in \mathbb{R}^2 : |x_1 - 0.6| < 0.45, |x_2 + 0.6| < 0.25\}, \\
D &= \text{disk} \cup \text{rectangle}, \\
\eta(x) &= 0.5 \quad \text{in } D.
\end{aligned}$$

c) Square-shaped object with cavity

$$\begin{aligned}
\text{cavity} &= \{(x_1, x_2)^\top \in \mathbb{R}^2 : x_1^2 + x_2^2 < 0.3^2\}, \\
\text{square} &= \{(x_1, x_2)^\top \in \mathbb{R}^2 : |x_1| < 0.5, |x_2| < 0.5\}, \\
D &= \text{square} \setminus \overline{\text{cavity}}, \\
\eta(x) &= 1 \quad \text{in } D.
\end{aligned}$$

To generate the scattering data for the numerical examples, we solve the Lippmann-Schwinger equation (5) using a spectral Galerkin method developed in [20]. Using N_d incident plane waves and measuring the data at N_x points on $\partial\Omega$, the Cauchy data $u_{\text{sc}}(x, d)$, $\partial u_{\text{sc}}/\partial\nu(x, d)$, where $(x, d) \in \partial\Omega \times \mathbb{S}$, are then $N_d \times N_x$ matrices. We add artificial noise to these data as follows. Two complex-valued noise matrices $\mathcal{N}_{1,2}$ containing random numbers that are uniformly distributed in the complex square

$$\{a + ib : |a| \leq 1, |b| \leq 1\} \subset \mathbb{C}$$

are added to the data matrices. For simplicity we consider the same noise level δ for both u_{sc} and $\partial u_{\text{sc}}/\partial\nu$. The noisy data u_{sc}^δ and $\partial u_{\text{sc}}^\delta/\partial\nu$ are given by

$$\begin{aligned}
u_{\text{sc}}^\delta &:= u_{\text{sc}} + \delta \frac{\mathcal{N}_1}{\|\mathcal{N}_1\|_F} \|u_{\text{sc}}\|_F, \\
\frac{\partial u_{\text{sc}}^\delta}{\partial\nu} &:= \frac{\partial u_{\text{sc}}}{\partial\nu} + \delta \frac{\mathcal{N}_2}{\|\mathcal{N}_2\|_F} \left\| \frac{\partial u_{\text{sc}}}{\partial\nu} \right\|_F,
\end{aligned}$$

where $\|\cdot\|_F$ is the Frobenius matrix norm.

5.1 Reconstruction with different wave numbers (Figure 1)

We present in Figure 2 reconstruction results for the wave numbers $k = 4$ (wavelength ≈ 1.57) and $k = 8$ (wavelength ≈ 0.78). The data are near-field Cauchy data with 30% noise. We use $N_x \times N_d = 64 \times 64$ for the kite-shaped object and disk-and-rectangle object, while the square-shaped object with cavity is examined with $N_x \times N_d = 96 \times 96$. It can be seen from the Figure 1 that the reconstruction results are improved with a larger value of k . We also see that the two imaging functionals can image very well the square-shaped object with cavity. It is interesting that this object violates the assumption that $\mathbb{R}^n \setminus \overline{D}$ must be connected when studying the well-posedness of the direct scattering problem (1)–(3).

5.2 Reconstruction with highly noisy data (Figure 2)

We present in Figure 2 reconstruction results for near-field Cauchy data perturbed by 60% and 90% noise. The wave number $k = 8$ and again we use $N_x \times N_d = 64 \times 64$ for the kite-shaped object and disk-and-rectangle object, and $N_x \times N_d = 96 \times 96$ for the square-shaped object with cavity. Although we can notice some deterioration in the case of 90% noise, the reconstructions are still pretty reasonable. These results show that both imaging functionals $I(z)$ and $I_2(z)$ are extremely robust with respect to noise in the data. We have also observed this robustness in the orthogonality sampling method for Maxwell's equations, see [12].

5.3 Reconstruction with far-field data (Figure 3)

The focus of this example is to examine the performance of the imaging functionals $I(z)$, $I_{\text{far}}(z)$, defined by (16), $I_{2,\text{far}}(z)$, defined in (20), in the case of far-field data with 30% noise. We recall that $I_{\text{far}}(z)$ and $I_{2,\text{far}}(z)$ use only u_{sc} instead of the Cauchy data. Again we consider $k = 8$ and the size $N_x \times N_d$ of the data matrices are the same as in the previous examples. As mentioned at the beginning of this section the far-field data are measured on $\partial\Omega$ that is the circle of radius $R = 100$ (about 125 wavelengths away from the scattering objects). We can see in Figure 3 that the reconstruction results with far-field data are as good as those with the near-field data. The results for $I_2(z)$ are similar to those of $I_{2,\text{far}}(z)$ so they are skipped to avoid repetitions.

5.4 Reconstruction with partial data (Figure 4)

In this last example we consider the case of near-field data for a half-circle aperture (again 30% noise). More precisely, we consider the Cauchy data $u_{\text{sc}}(x, d), \partial u_{\text{sc}}/\partial \nu(x, d)$, where

$$x = (3 \cos(\theta), 3 \sin(\theta))^\top, \quad d = (\cos(\theta), \sin(\theta))^\top, \quad \pi \leq \theta \leq 2\pi.$$

That means the incident plane waves illuminate with direction vectors of propagation varying on the bottom half of \mathbb{S} , and the Cauchy data are given on the bottom half of the measurement circle $\partial\Omega$. Moreover, the number of data points N_x and incident plane waves N_d are also half of those

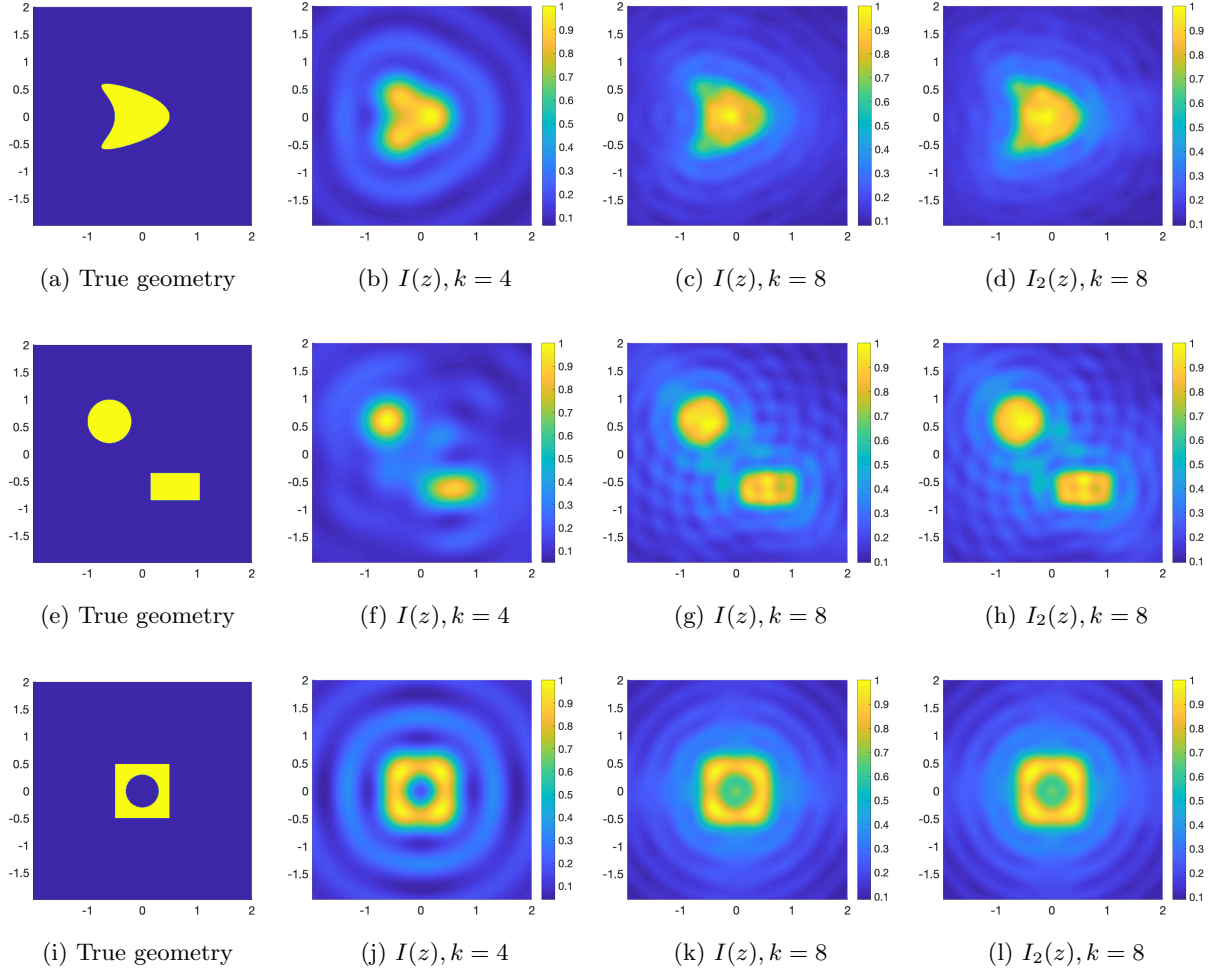


Figure 1: Reconstruction with near-field Cauchy data for different wave numbers. There is 30% noise added to the data ($\delta = 0.3$). First column (a, e, i): true geometry. Second column (b, f, j): reconstructions with $I(z)$ and $k = 4$. Third column (c, g, k): reconstructions with $I(z)$ and $k = 8$. Last column (d, h, l): reconstructions with $I_2(z)$ and $k = 8$.

of the full data case, that means $N_x \times N_d = 32 \times 32$ for the kite-shaped object and disk-and-rectangle object, and $N_x \times N_d = 48 \times 48$ for the square-shaped object with cavity. As it can be seen from Figure 4, the reconstruction results for the first two objects are still pretty reasonable. However, the shape of the reconstructed square-shaped object with cavity is no longer accurate. This object is certainly more difficult to image compared with the first two objects.

Acknowledgement. The author is partially supported by NSF grant DMS-1812693.

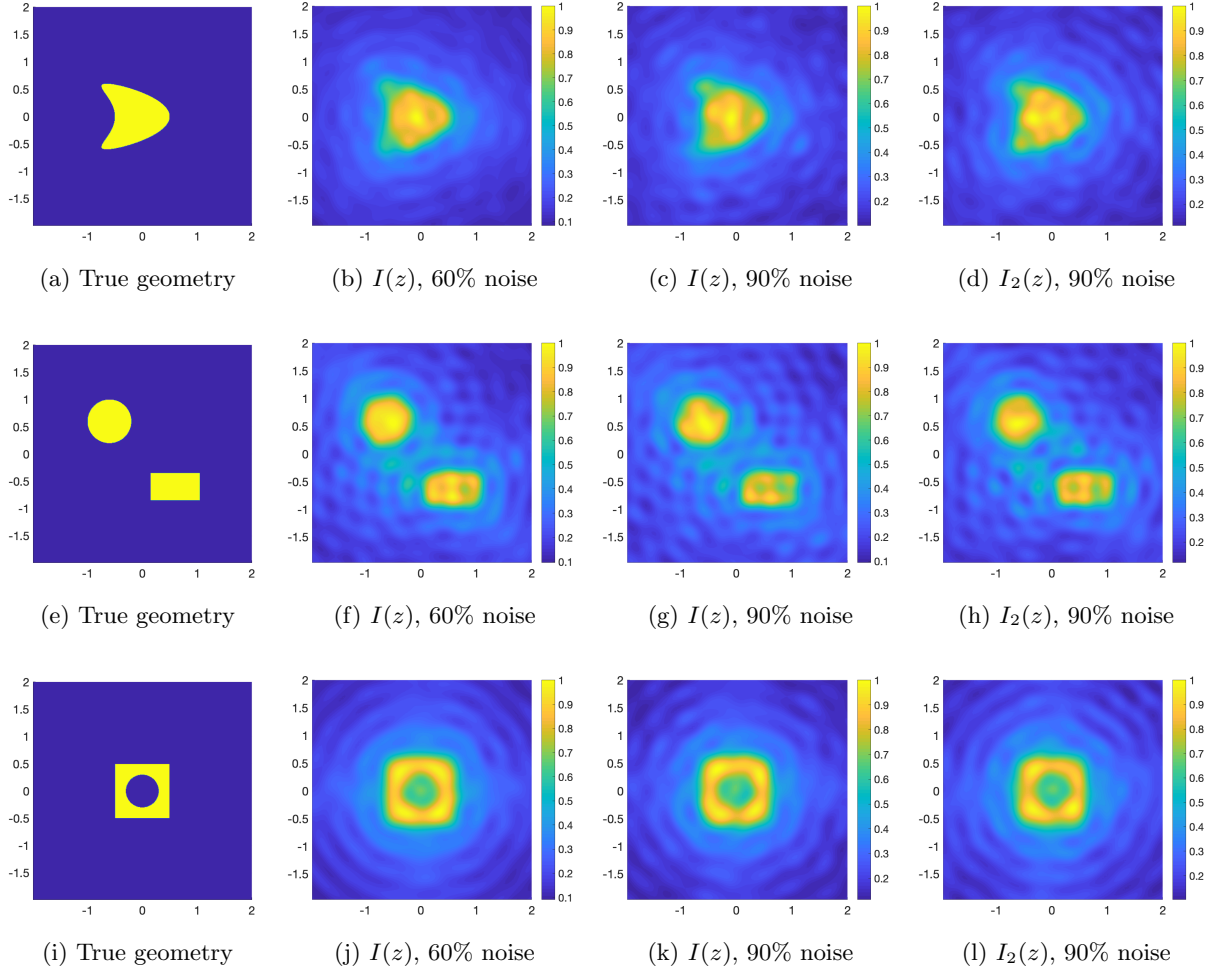


Figure 2: Reconstruction with highly noisy near-field data. Wave number $k = 8$. First column (a, e, i): true geometry. Second column (b, f, j): reconstructions with 60% noise using $I(z)$. Third column (c, g, k): reconstructions with 90% noise using $I(z)$. Last column (d, h, l): reconstructions with 90% noise using $I_2(z)$.

References

- [1] M. Akinci, M. Cayoren, and I. Akduman. Near-field orthogonality sampling method for microwave imaging: Theory and experimental verification. *IEEE Trans. Microw. Theory Tech.*, 64:2489, 2016.
- [2] L. Audibert and H. Haddar. A generalized formulation of the linear sampling method with exact characterization of targets in terms of farfield measurements. *Inverse Problems*, 30:035011, 2014.

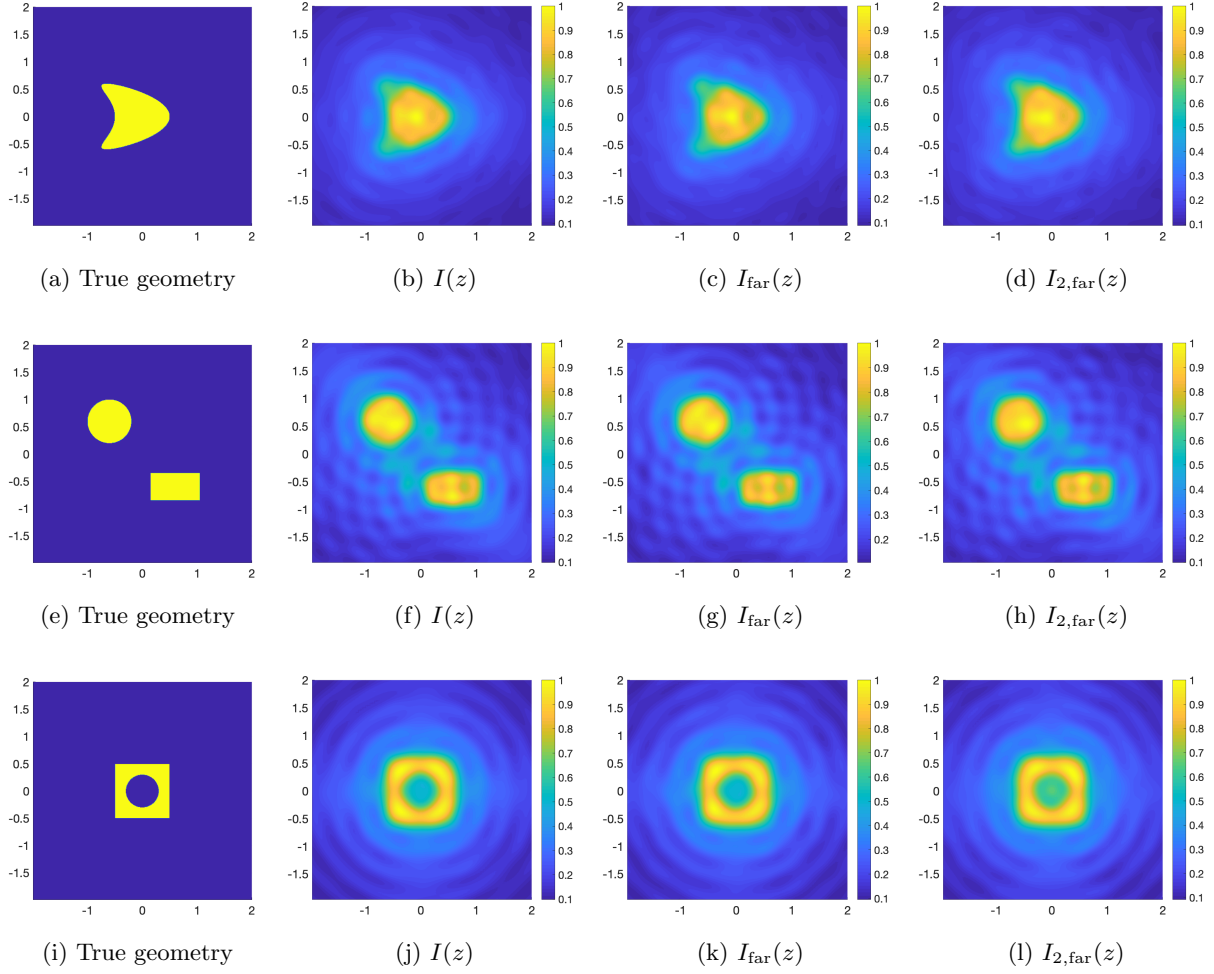


Figure 3: Reconstruction with far-field data. There is 30% noise added to the data, $k = 8$. First column (a, e, i): true geometry. Second column (b, f, j): reconstructions using $I(z)$. Third column (c, g, k): reconstructions using $I_{\text{far}}(z)$. Last column (d, h, l): reconstructions using $I_{2,\text{far}}(z)$.

- [3] F. Cakoni, D. Colton, and H. Haddar. *Inverse Scattering Theory and Transmission Eigenvalues*. SIAM, 2016.
- [4] F. Cakoni, D. Colton, and P. Monk. *The Linear Sampling Method in Inverse Electromagnetic Scattering*. SIAM, 2011.
- [5] J. Chen, Z. Chen, and G. Huang. Reverse time migration for extended obstacles: acoustic waves. *Inverse Problems*, 29:085005, 2013.
- [6] D. Colton, J. Coyle, and P. Monk. Recent developments in inverse acoustic scattering theory. *SIAM Review*, 42:396–414, 2000.

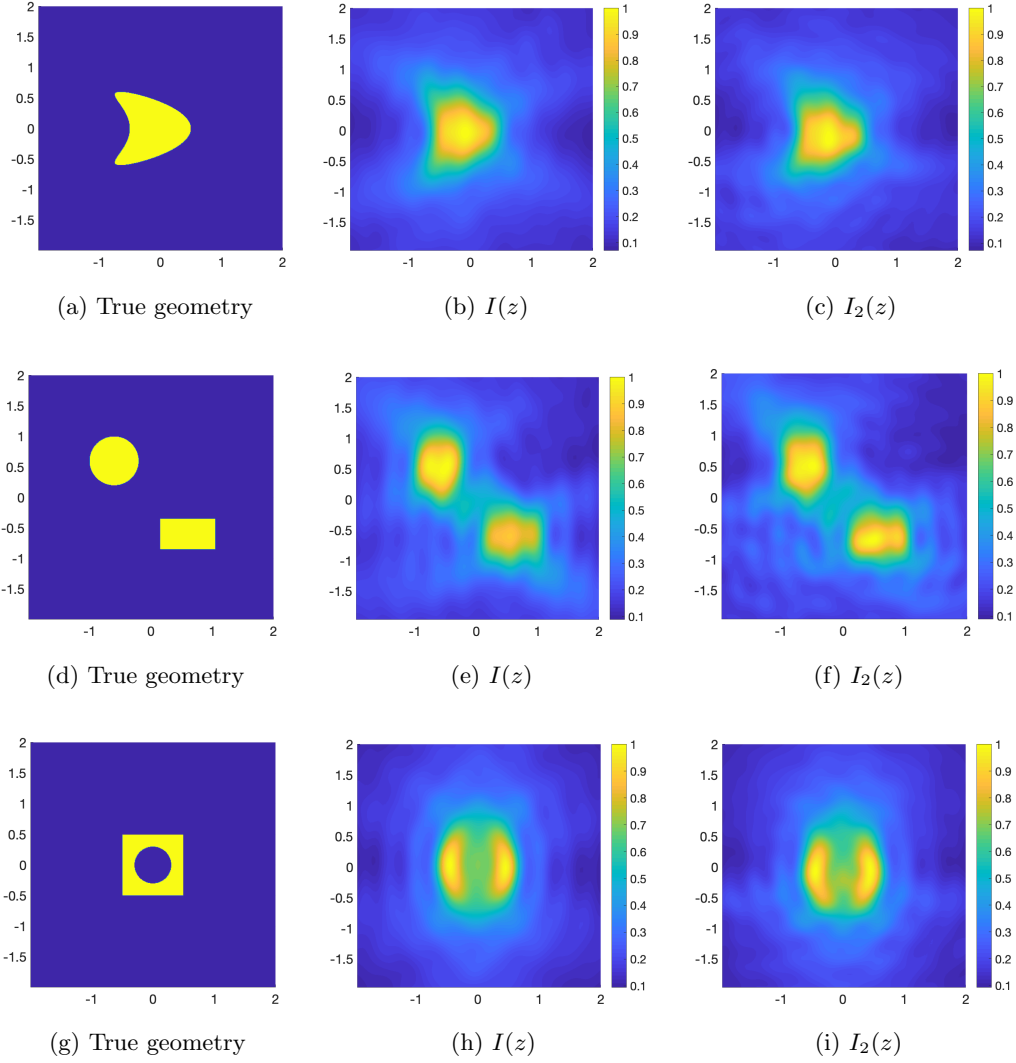


Figure 4: Reconstruction with partial near-field data (bottom half-circle aperture). There is 30% noise added to the data, $k = 8$. First column (a, d, g): true geometry. Second column (b, e, h): reconstructions using $I(z)$. Last column (c, f, i): reconstructions using $I_2(z)$.

- [7] D. Colton and A. Kirsch. A simple method for solving inverse scattering problems in the resonance region. *Inverse Problems*, 12:383–393, 1996.
- [8] D. Colton and R. Kress. *Inverse Acoustic and Electromagnetic Scattering Theory*. Springer, New York, 3rd edition, 2013.
- [9] J. Garnier and G. Papanicolaou. *Passive Imaging with Ambient Noise*. Cambridge University Press, Cambridge, 2016.

- [10] R. Griesmaier. Multi-frequency orthogonality sampling for inverse obstacle scattering problems. *Inverse Problems*, 27:085005, 2008.
- [11] I. Harris and A. Kleefeld. Analysis of new direct sampling indicators for far-field measurements. *Inverse Problems*, 35:054002, 2019.
- [12] I. Harris and D.-L. Nguyen. Orthogonality sampling method for the electromagnetic inverse scattering problem. *SIAM J. Sci. Comput.*, 42:B72–B737, 2020.
- [13] M. Ikehata. Reconstruction of the shape of the inclusion by boundary measurements. *Commun. Part. Diff. Eq.*, 23:1459–1474, 1998.
- [14] K. Ito, B. Jin, and J. Zou. A direct sampling method to an inverse medium scattering problem. *Inverse Problems*, 28:025003, 2012.
- [15] K. Ito, B. Jin, and J. Zou. A direct sampling method for inverse electromagnetic medium scattering. *Inverse Problems*, 29:095018, 2013.
- [16] X. Ji, X. Liu, and B. Zhang. Inverse acoustic scattering with phaseless far field data: Uniqueness, phase retrieval, and direct sampling methods. *SIAM J. Imaging Sci.*, 12:1163–1189, 2019.
- [17] S. Kang, M. Lambert, and W.-K. Park. Direct sampling method for imaging small dielectric inhomogeneities: analysis and improvement. *Inverse Problems*, 34:095005, 2018.
- [18] A. Kirsch. Characterization of the shape of a scattering obstacle using the spectral data of the far field operator. *Inverse Problems*, 14:1489–1512, 1998.
- [19] A. Kirsch and N.I. Grinberg. *The Factorization Method for Inverse Problems*. Oxford Lecture Series in Mathematics and its Applications 36. Oxford University Press, 2008.
- [20] A. Lechleiter and D.-L. Nguyen. A trigonometric Galerkin method for volume integral equations arising in TM grating scattering. *Adv. Comput. Math.*, 40:1–25, 2014.
- [21] X. Liu. A novel sampling method for multiple multiscale targets from scattering amplitudes at a fixed frequency. *Inverse Problems*, 33:085011, 2017.
- [22] D.-L. Nguyen. Direct and inverse electromagnetic scattering problems for bi-anisotropic media. *Inverse Problems*, 35:124001, 2019.
- [23] W.-K. Park. Direct sampling method for retrieving small perfectly conducting cracks. *J. Comput. Phys.*, 373:648–661, 2018.
- [24] R. Potthast. A fast new method to solve inverse scattering problems. *Inverse Problems*, 12:731–742, 1996.
- [25] R. Potthast. A survey on sampling and probe methods for inverse problems. *Inverse Problems*, 22:R1–R47, 2006.
- [26] R. Potthast. A study on orthogonality sampling. *Inverse Problems*, 26:074015, 2010.